

A Beamwidth and Steering Reconfigurable Active Integrated Metasurface Antenna for Dynamic Radiation Control

Tian Liang, *Student Member, IEEE*, Zhan Wang, *Student Member, IEEE*,
and Yuandan Dong, *Senior Member, IEEE*

Abstract—In this paper, a beamwidth and pattern-steering reconfigurable active integrated antenna (AiA) is proposed and studied in 2.4 GHz band. Two low noise amplifiers (LNAs) are applied as the switches to control the beamwidth in this work. Owing to their high on/off state transmission ratio, using amplifiers as switches is an economic and easy way to realize excellent reconfigurability. An aperture coupled metasurface contributes to a unified radiation pattern and reflection coefficient. To highlight the applications, a pair of switchable phase shifters is cascaded to the amplifiers to realize beam steering. The coupling scheme of the AiA is illustrated which exhibits a quasi-duplex communication function. Power compression and third-order intermodulation of the AiA are discussed and measured. The impedance bandwidth fully covers the range from 2.2GHz to 2.7GHz. The measured tunable range of the beamwidth is from 111° to 32° and the beam steering angle is from -39° to 36° in the E-plane. The measured peak system gain is 14.7 dBi, while under the passive mode it is 6.8 dBi. The peak system efficiency is measured up to 220 % for the active mode and 80% for the passive mode. The peak power added efficiency of the active mode is 40.4 %. The measurement results agree well with the simulation.

Index Terms—Active integrated antenna (AiA), beamwidth reconfigurable, beam steering reconfigurable, low noise amplifier (LNA), noise figure (NF), nonlinearity, quasi-duplexing.

I. INTRODUCTION

THE boom of the Internet of Things (IoTs) devices congests the ISM bands, especially the 2.4 GHz and 5 GHz bands. Crowded channels severely deteriorate the electromagnetic environment and lead to unwanted connection interruption. To overcome this problem, increasing transmission power is the conventional way to improve the connection quality. However, it contradicts the low-power requirement of the IoT devices, especially for devices powered by batteries. Introducing the reconfigurable antennas is another solution which attracts substantial attention and research [1]. Diverse frequency tunable and beam steering reconfigurable antennas are designed to optimize the connection quality. For the 5G system,

half-power beamwidth (HPBW) reconfigurability is also anticipated [2]. In a crowd scenario, a high directivity antenna with beam steering characteristic decreases the mutual interference of nodes and accordingly allows dense base station configuration and better coverage. The overall communication capability is improved. In contrast, in a sparse scenario, such as grassland, a broad HPBW and low directivity antenna supports wide-range communication with fewer nodes.

For frequency or pattern reconfigurable antennas, reconfigurable components are usually loaded to tune the resonant modes of the antenna while the radiation aperture remains the same for most of the time [3]–[5]. The unintentional aperture variation occurs mostly in pattern reconfigurable antennas when tuning the coupled microstrip. The phenomenon is common among the pattern reconfigurable antenna based on Yagi-Uda antenna, which uses reflectors to control backward radiation and realize beam steering [1], [6].

In contrast, the key to control the HPBW is tuning the effective antenna radiation aperture. The first way to achieve HPBW reconfigurability is to introduce a Yagi-like structure to alter the aperture [1], [7]–[11]. In [7], the metal strips controlled by the PIN diodes act as the reflectors. The reflector suppresses the sideward radiation, improves the directivity, and narrows the HPBW. Thus, applying reflectors is the most common way to obtain HPBW reconfigurability and beam steering. The second method is to apply a phaser to shape the pattern [12]–[14]. The in-phase or out-of-phase configurations add or cancel the radiated fields and affect the effective radiation aperture, which controls the antenna gain and HPBW simultaneously. In [14], three radiated elements with only one phaser are combined to obtain beamwidth reconfigurability. The work obtains increased tuning range of the HPBW while losing the beam steering reconfigurability as a trade-off. Another design using a partially reflective surface (PRS) is shown in [15]. The antenna realizes beam scanning and HPBW reconfigurability at the same time, while the complicated PRS controlling impedes it putting into the wide application.

As the trend of integrated designs, amplifiers are introduced to antenna designs to compose the active integrated antennas (AiAs). Usually the integrated design is able to provide both miniaturization and performance improvement. A series of AiAs embed the amplifiers in antenna structure to realize oscillated radiators [16]–[18], active multipliers [19], [20], amplifier antennas for TX [21]–[26], and RX [27]–[30]. For TX,

Manuscript received Sept. 8th, 2021; Revised **; This work was supported by the National Natural Science Foundation of China under Contract 62171091 and 62161160310. (Corresponding author: Yuandan Dong).

The authors are with the School of Electronic Science and Engineering, University of Electronic Science and Technology of China (UESTC), Chengdu 611731, China. (ydong@uestc.edu.cn).

Color versions of one or more of the figures in this paper are available online at <http://ieeexplore.ieee.org>.

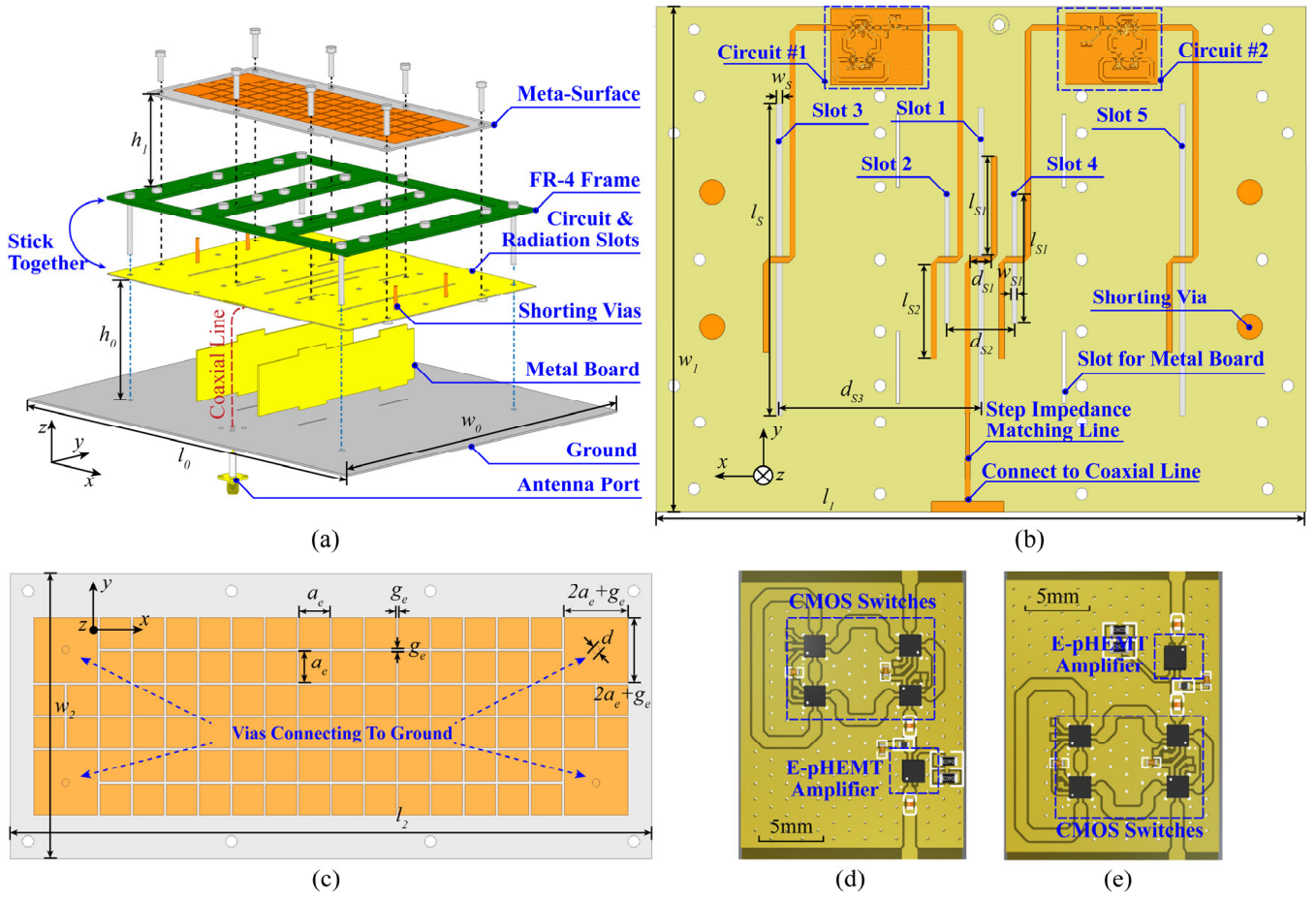


Fig. 1 Antenna structure. (a) The overview of the assembled scheme of the reconfigurable AiA, (b) bottom view of the circuit layer, (c) top view of the metasurface antenna, (d) enlarged bottom view of the Circuit #1, and (e) enlarged bottom view of the Circuit #2.

AiAs shorten the feeding line between amplifiers and antennas which minimizes the power loss. In contrast, the RX AiAs function as the input and/or output matching network of the antenna, which decreases the transmission line (TL) loss, improves the signal-to-noise ratio and greatly simplifies the bill of the material (BOM) of the design [21], [23]. Besides, antennas as the component that cannot be designed much smaller than a wavelength. They have enough surface area to dissipate the heat produced by the amplifiers. Therefore, AiAs draw increasing attention and application.

In this paper, two amplifiers are used to serve as the high-performance switches to tune the HPBW of the reconfigurable AiA, which is operated at 2.4 GHz. Both signal amplification and reconfigurability are simultaneously achieved. The design theory and considerations are summarized in Section II. The antenna keeps a passive channel and performs quasi-duplexing capability, which means the antenna supports receiving function even in the active mode. A CMOS switch phased network connects to the amplifiers and realizes beam steering. The AiA can be switched between the three active modes and a passive mode, providing a reconfigurable gain to the system. Simulation and measurement results are accordingly given in Section III. Section IV presents the working scenario of the AiA and discusses how the reconfigurable AiA improves system performance and achieves dynamic power consumption. Finally, a comparison to the

previous works is presented in Section V and a brief conclusion is drawn in Section VI.

II. WORKING MECHANISM AND ANTENNA TOPOLOGY

A. The geometry of the Antenna

The geometry of the antenna is shown in Fig. 1 (a). Starting from the bottom, the antenna consists of a metal ground plane, a pair of vertical isolation metal boards, a printed circuit board (PCB) with an FR-4 frame, and a metasurface above the radiation slots. To resist backward radiation, a metal ground plane is applied which contributes to the high antenna gain. The ground is fabricated using a 1 mm brass plate, which supports the antenna. Two FR-4 PCBs with dense metalized holes are used to precisely fabricate the vertical metal boards. The two boards decouple the three antenna elements and the working mechanism is discussed in Section II.D. Circuit and radiation slots are etched on a PCB made up of F4BME220 substrate, which is low-cost and low-loss (thickness = 0.508 mm, $\epsilon_r = 2.2$, $\tan \delta = 0.001$). Fig. 1 (b) illustrates the details of the circuit with a bottom view. The characteristic impedance of the transmission line is 50 Ω . The feeding line of the antenna is a microstrip line for easy tuning. A microstrip line to a coplanar waveguide with ground (CPWG) structure is applied to connect the LNAs and switches. The LNAs are TQP3M9035, an E-pHEMT with internal matching circuit. TABLE I

TABLE I KEY PARAMETERS OF THE AMPLIFIER @ 2.4GHZ (UNIT: dB)

	S_{11}	S_{21}	S_{12}	S_{22}	NF	P_{1dB}	Output IP3
On state	-13.9	15.6	-26.3	-9.3	0.9	23.2dBm	37.3dBm
Off state	-0.8	-20.7	-20.8	-2.7	-	-	-

TABLE II KEY DIMENSION PARAMETERS OF THE ANTENNA (UNIT: MM)

w_0	l_0	h_0	h_1	w_1	l_1	d_{S1}	l_{S1}	w_S	l_S
200	240	27	10	140	180	7.35	27.8	1.60	86.3
l_{S2}	d_{S2}	d_{S3}	w_2	l_2	a_e	g_e	d	w_{S1}	l_{S1}
26.9	18.7	46.4	80	180	8.6	0.65	2	1.38	35.9

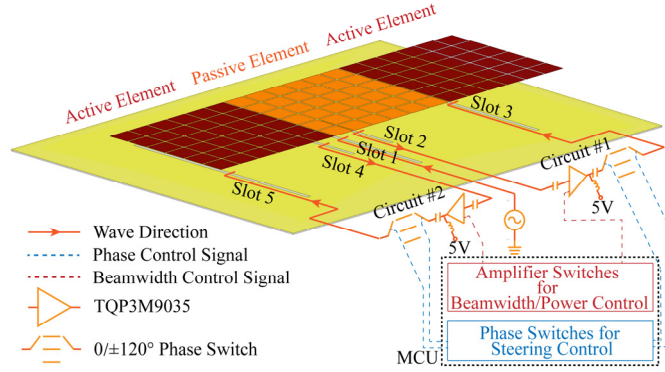


Fig. 2 Circuit schematic with connection to the EM model of the proposed active reconfigurable antenna.

TABLE III RECONFIGURATION MODE SUMMARY

Reconfiguration	Beam Steering on E-Plane (°)	HPBW on E-Plane (°)	Peak System Gain (dBi)
Mode 0	0	105	8.0
Mode 1	0	38	14.2
Mode 2	-36	32	15.4
Mode 3	36	32	15.4

summarizes the key parameter of the TQP3M9035 [31]. The switches of the phaser are PE42422 in the CMOS process. A segment stepped-impedance microstrip line is loaded near the feeding line for broad bandwidth impedance matching. An FR-4 frame is attached to the PCB to strengthen the structure. Radiation slots are etched on the opposite of the circuit to excite the metasurface. Three radiated slots, Slot 1, Slot 3, Slot 5, have identical parameters. Coupled Slot 2, Slot 4 also have the same parameters. The key design parameters of the proposed antenna are given in TABLE II.

B. Power Distribution Topology

The circuit schematic with the EM model of the proposed antenna is shown in Fig. 2. The EM and circuit simulation are done separately and then synthesized based on scattering parameters. The synthesis can be done in commercial software such as HFSS and CST. Three apertures contribute to the far-field radiation. The antenna shows four reconfigurable modes by controlling the amplitude and the phase distribution on the radiation aperture. The modes are summarized in TABLE III. The gain variation mainly comes from the low return loss of the output port of the amplifiers. To evaluate the gain of the reconfigurable AiA, system gain is defined as:

$$G_{system} = \frac{4\pi U(\theta, \phi)}{P_0} \quad (1)$$

where $U(\theta, \phi)$ is the radiation intensity in the far-field zone; P_0 is the incident power.

In Mode 0, the LNAs are set to shut down mode and the input impedance of the amplifiers approximates short-circuit. It means Slot 2 and Slot 4 couple little energy to Circuit #1 and Circuit #2. Only Slot 1 contributes to the radiation. Thus, the antenna is purely passive in Mode 0 and performs lower gain, broad beamwidth, and full-duplex communication.

In Mode 1, Mode 2, and Mode 3, most of the input power excites the metasurface and radiates into space directly through Slot 1, while a power of -15 dB couples to Circuit #1 and Circuit #2 by Slot 2 and Slot 4, respectively. Considering the loss of the TL, Circuit #1 and Circuit #2 amplify the signals with a gain of +15dB. The circuits also modify the excitation phase (β). The β of the Mode 1, Mode 2, and Mode 3 is switched to 0° , -120° , $+120^\circ$, respectively. The phased signals excite Slot 3 and Slot 5 and contribute to the steering far-field radiation on the E-plane (XOZ-plane). The amplifiers increase the total radiation power and raise the system gain. The HPBW is narrowed to about 32° for each mode. Although the gain improvement is only validated in the transmission direction, the AiA supports bidirectional communication, since the radiation Slot 1 is purely passive. This property is defined as quasi-duplexing and is quite novel among the AiA designs.

C. Working Mechanism of Beamwidth Reconfigurability

To achieve active integration and reconfigurable beamwidth simultaneously, two LNAs are adopted as the core reconfigurable elements to control the aperture. The TQP3M9035 provides a special pin that enables/disables the internal bias, so no additional control circuit is needed. A performance discussion by using LNAs as switches is provided below.

The HPBW of the antenna is sensitive to the excitation power around the edge of the aperture. A simplified model that only composed Slot 1, Slot 3, and Slot 5, is applied to elaborate this feature. The three slots are independently excited with the following power ratio:

$$\frac{P_{Slot1}}{P_{Slot3}} = \frac{P_{Slot1}}{P_{Slot5}} = \mu \quad (2)$$

When μ is swept logarithmically from 0 dB to 40 dB, the normalized radiation pattern on the E-plane is obtained and the result is given in Fig. 3. The HPBW region is highlighted by a dash-dot line. It can be learned that the HPBW varies dramatically when μ is lower than 30 dB while remaining relatively stable when μ exceeds 30 dB. Thus, a reconfigurable circuit that can obtain a μ higher than 30 dB is crucial for beamwidth reconfigurable applications.

For the passive series switches, such as PIN diodes and CMOS switches, the figure of merit (FoM) is the conventional parameter to evaluate the performance of the switch [32]. The equivalent circuit model of the passive switch is shown in Fig. 4. The impedance ratio of the switch in On-State and Off-State is:

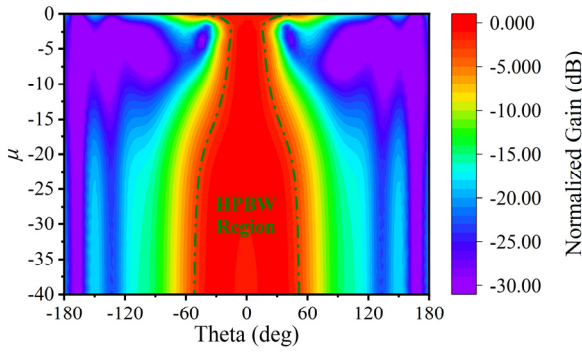
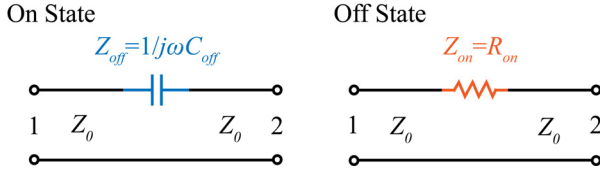
Fig. 3 Normalized radiation pattern on the E-plane with different μ .

Fig. 4 Equivalent circuit schematic of the passive switch.

TABLE IV PTR COMPARISON OF SWITCHES @ 2.4GHz

Device	Type	S_{21}^{on} (dB)	S_{21}^{off} (dB)	Switch Time	PTR (dB)
SMP1345	PIN	-1.5 @10mA	-15.0		13.5
BAR50-02L	PIN	-0.3 @10mA	-17.5		17.2
BAR64-03W	PIN	-0.4 @10mA	-13.0		12.6
PE42422	CMOS	-0.4	-29.0	2us	28.6
SKY13699-21	CMOS	-0.3	-38		37.7
ADGM1304	MEMS	-0.3	-24	75us	23.7
TQP3M9035	pHEMT	15.6	-20.7	165ns	36.3

$$Z_{ratio} = \frac{Z_{on}}{Z_{off}} = j\omega R_{on} C_{off} \quad (3)$$

The FoM is defined as the product of the R_{on} and C_{off} , which is in the form of a time constant [32]. However, when evaluating the active switches, such as amplifiers, the equivalent negative output resistor results in a negative FoM so the formula (3) is unsuitable for active switches. To overcome this problem, we define the power transmission ratio (PTR) between the two switch states to unified study the property of the active and passive switches. The PTR is written as:

$$PTR = \frac{|S_{21}^{on}|}{|S_{21}^{off}|} \quad (4)$$

For the passive switches, the PTR of the equivalent circuit shown in Fig. 4 can be simplified as:

$$PTR_{passive} = \frac{\left| \frac{2Z_0}{R_{on} + 2Z_0} \right|}{\left| \frac{j\omega C_{off} 2Z_0}{1 + j\omega C_{off} 2Z_0} \right|} = \frac{|1 + j\omega C_{off} 2Z_0|}{|R_{on} + 2Z_0| |j\omega C_{off}|} \quad (5)$$

The characteristic impedance (Z_0) of the TL is unexpected in describing the switch performance since it is not an intrinsic parameter of the switches. Therefore, the limitation of the PTR is that it only suits the discussion of a system with specified Z_0 .

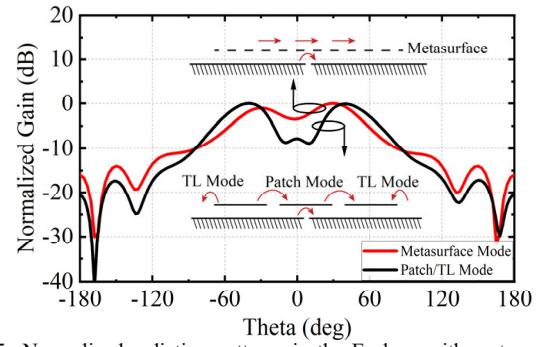


Fig. 5 Normalized radiation patterns in the E-plane with metasurface and coupled patch elements.

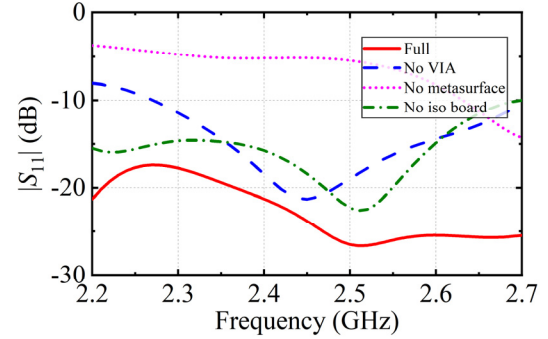


Fig. 6 Comparison of the reflection coefficient between the complete structure and the structure without shorting vias, metasurface, and isolation board.

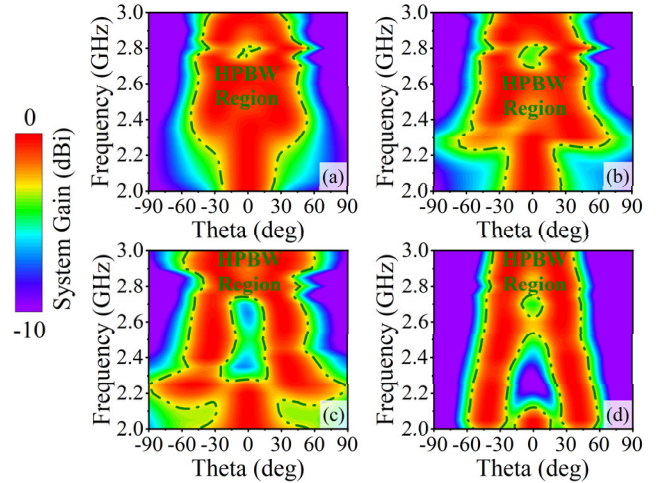


Fig. 7 Comparison of the Mode 0 radiation patterns with (a) Complete structure, (b) The structure without the shorting vias, (c) The structure without the metasurface, and (d) The structure without the isolation board.

For example, the Z_0 is 50Ω in this article. PTR can be easily measured by the vector network analyzer (VNA) or acquired through the manufacture datasheets.

The PTR of several switches with different fabrication processes is summarized in TABLE IV at 2.4 GHz. It can be noticed that the S_{21}^{off} of the LNA is similar to other kinds of switches but the S_{21}^{on} is significantly higher. This property provides high achievable PTR. In this paper, we define that $\mu = 0$ dB denotes the switches are set to On-state, while higher μ represents the Off-state of the switches. Thus, the high PTR LNA can provide a μ significantly higher than 30 dB and is

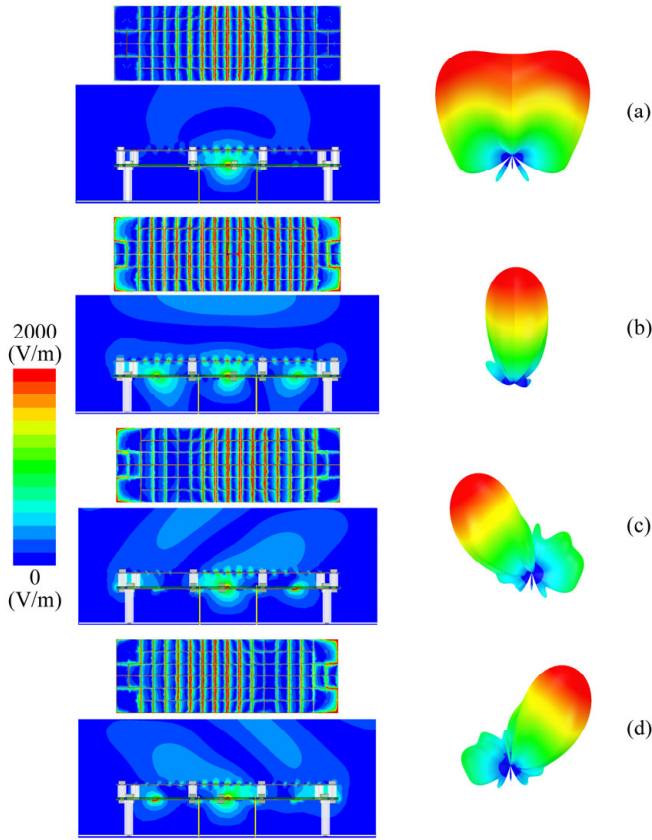


Fig. 8 E-field distribution and radiation patterns for each configuration. (a) Mode 0, (b) Mode 1, (c) Mode 2, (d) Mode 3.

suitable for composing AiA design. Besides, the fast switch time also benefits our work, which is rarely mentioned in other reconfigurable antenna designs. In conclusion, using amplifiers as switches is a low-cost scheme that satisfies the reconfigurable AiA applications.

D. Improving the Performance of Mode 0

To improve the reflection coefficient [33] and flatten the radiation pattern of Mode 0, the work incorporates four designed structures, which include the metasurface above the radiation slots, the four vias at the corner of the metasurface, and the two isolation boards. In comparison to applying a patch radiator, the metasurface does not excite transmission line mode, as shown in Fig. 5. Thus, it is easy to realize a uniform broad radiation pattern. The influence of the structures on the beamwidth and reflection coefficient in the whole working band is discussed in the following.

A comparison graph of the simulated $|S_{11}|$ is given in Fig. 6 to explain the effectiveness of the structures. It can be learned that the metasurface improves the impedance bandwidth in the whole band. The vias affect the reflection coefficient in both the high band and the low band. In contrast, the isolation board only affects the high operation band.

The normalized radiation pattern of Mode 0 is shown in Fig. 7. Comparing Fig. 7 (a) and (b), the removal of the shorting vias has a relatively weak influence on the radiation pattern. However, the removal of the metasurface leads to a split HPBW in the center of the operation band (Fig. 7 (c)). Fig. 7 (d) shows that the isolation boards avoid split radiation patterns in the low-frequency band. The isolation boards

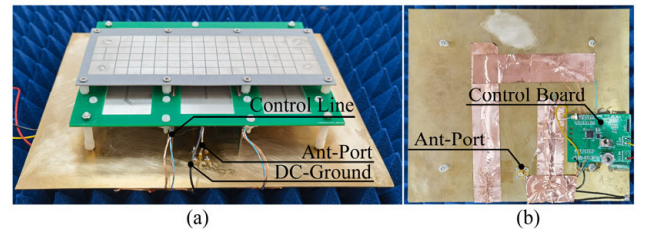


Fig. 9 Photograph of the fabricated reconfigurable AiA. (a) Front view, and (b) Back view.

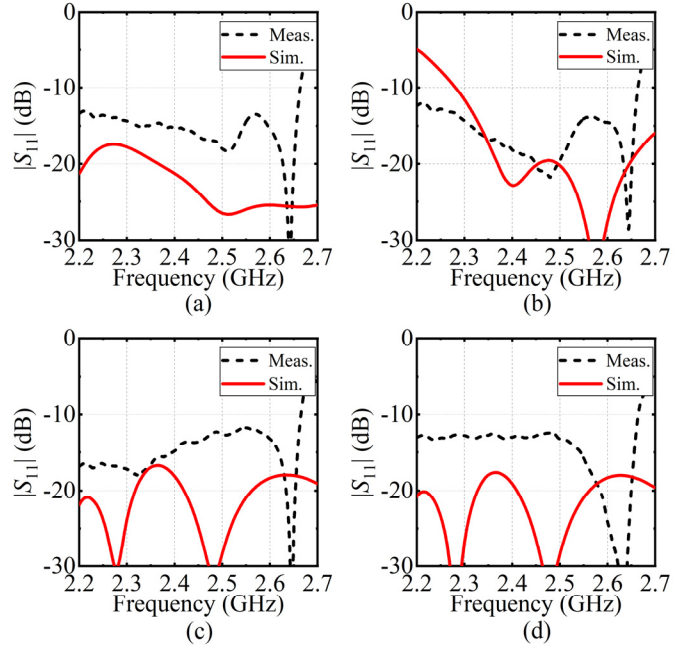


Fig. 10 Simulated and measured reflection coefficient of the antenna. (a) Mode 0, (b) Mode 1, (c) Mode 2, and (d) Mode 3.

decouple the three radiation slots and the radiation patterns can be stably controlled by the circuits. The E-field distribution of Mode 0 is shown in Fig. 8 (a). A uniform spherical wave can be observed above the metasurface. The simulated E-field distributions for Mode 1, Mode 2, and Mode 3 are also given in Fig. 8.

III. ANTENNA PERFORMANCE AND DISCUSSION

The reconfigurable AiA is fabricated for verification and the photos are given in Fig. 9. A control board composing an STM32 microcontroller is attached to the back of the metal ground. This small PCB board provides power supply and logic signal to the reconfigurable circuits. The scattering parameters of the components are obtained from the manufacturer for circuit level and electromagnetic field level co-simulation. ANSYS HFSS and Circuit simulator are applied in performing the co-simulation. The co-simulation improves the simulation accuracy of the scattering parameters and the radiation pattern. The scattering parameter is measured with a ZNB40 vector network analyzer. A StarLab Satimo near-field measurement system is applied to acquire the radiation patterns. Gain compression and third-order intermodulation measurements are realized with vector signal source and signal analyzer in a microwave chamber. Since the active modes only validate in transmission direction, the noise temperature has little

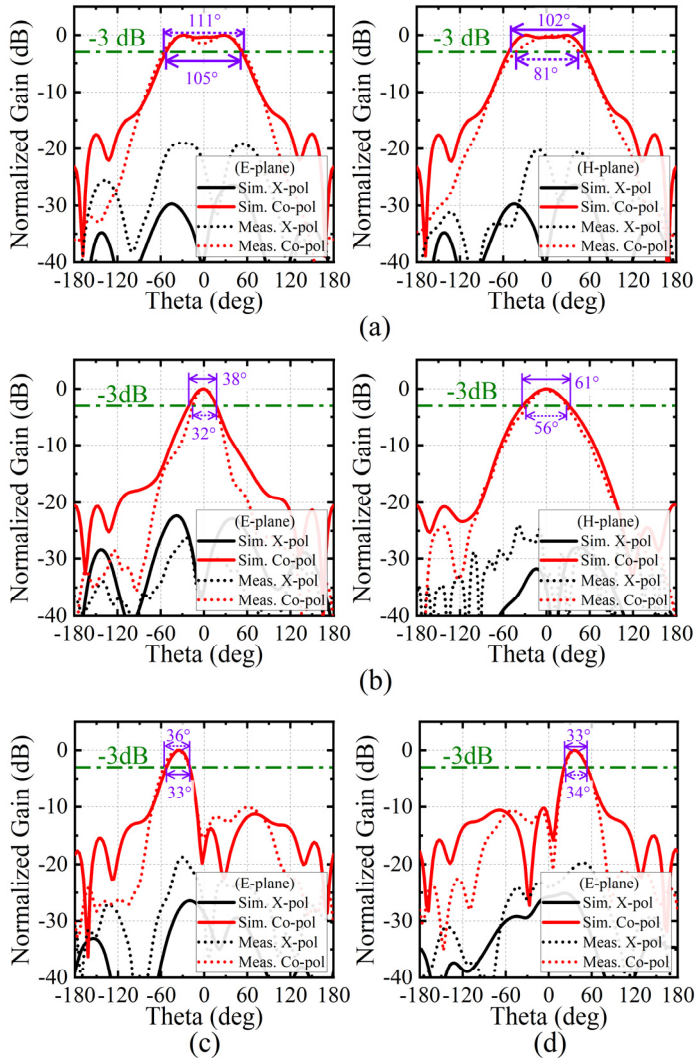


Fig. 11 Simulated and measured radiation patterns of the proposed antenna at 2.45 GHz for: (a) Mode 0 on E-plane and H-plane, (b) Mode 1 on E-plane and H-plane, (c) Mode 2 on E-plane, (d) Mode 3 on E-plane.

influence on the system performance and would not be discussed in this paper. The illustration of the antenna performance is given in this section.

A. Scattering Parameter

The antenna exhibits a broad impedance bandwidth. The simulated and measured scattering parameter is shown in Fig. 10. The combination of the broad bandwidth metasurface antenna and the LNA realizes a unified good reflection coefficient from 2.2 GHz to 2.7GHz. for each working mode. The simulated reflection coefficient of each mode is lower than -18 dB inside the IEEE 802.11 b/g/n band, while the measured result degenerates to -12 dB. The degeneration mainly comes from fabrication and assembly errors. Besides, the characteristic inconsistency of the component causes the variation between two active channels, and further causes the difference between Mode 2 and Mode 3, which can be found in Figs. 10 (c) and (d). Better reflection coefficient of the reconfigurable AiA can be obtained by a fine tune of the stepped-impedance matching line at the antenna excitation port.

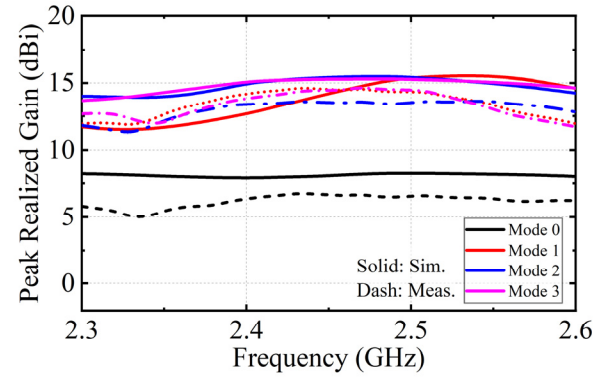


Fig. 12 Simulated and measured peak realized gain of the antenna. (a) Mode 0, (b) Mode 1, (c) Mode 2, and (d) Mode 3.

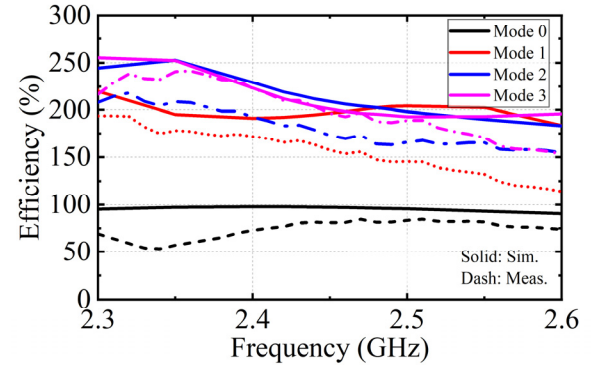


Fig. 13 Simulated and measured system efficiency of the AiA.

B. Radiation Pattern

The simulated and measured radiation patterns of the reconfigurable AiA 2.45 GHz are given in Fig. 11. The peak realized system gain of the antenna is given in Fig. 12. In Fig. 13, the system efficiency is accordingly presented. A little gain variation can be found between the modes. The error partially comes from the load-pull phenomenon of the amplifiers since the amplifiers work close to the compression point.

Fig. 11 (a) illustrates the radiation pattern in the E-plane and H-plane of Mode 0. On the E-plane, to obtain the broadest HPBW in this mode, the main lobe is designed to be about split. The simulated HPBW is 99°, while the measurement result is 110°. The simulated peak gain of the main lobe is 8.0 dBi and shows a relatively flat pattern. In contrast, the measured gain sinks 1.4 dB at the center of the beam. The peak gain drops to 6.7 dBi due to the efficiency degeneration. On the H-plane, the simulated HPBW is 102°. The according measured result is 81°. The antenna efficiency of the passive Mode 0 is tested at 80.8 %, while in the simulation it reaches 97.0 %. The measured cross-polarization radiation is lower than -20 dB and the trace shape agrees well with the simulation. However, the magnitude shows a little discrepancy, which is mainly due to the assembly height error of the metasurface.

The radiation patterns on the E-plane and H-plane of the active Mode 1 are presented in Fig. 11 (b). In this mode, both the directivity and the realized system gain of the antenna are evaluated. The maximum of the pattern points exactly at the

center point. On the E-plane, the simulated HPBW is 38° and the peak gain of the beam is 14.2 dBi. In contrast, the measured HPBW slightly narrows down to 32° . The variation mainly comes from the sharpen radiation beam brought by the manufacturing errors. It can also be noticed that the peak realized system gain of this mode is measured with 14.5 dBi, higher than the simulation result. This variation is due to that the fabricated antenna working band is slightly lower than that in the simulation. On the H-plane, the HPBW is simulated with 61° and measured with 56° . It means that the HPBW reconfigurability mainly appears on the E-plane and has a weak influence on the H-plane pattern. Due to the amplification of the LNAs, the reconfigurable AiA achieves a 157 % measured system efficiency. The narrow beamwidth mode exhibits -20 dB low cross-polarization radiation in comparison to the main lobe.

The radiation patterns of Mode 2 are presented in Fig. 11 (c), while the radiation patterns of Mode 3 are given in Fig. 11 (d). The cross-polarization is likewise 20 dB lower than the center beam. The simulation shows that on the E-plane, the main beam steers to -36° for Mode 2 while 36° for Mode 3. The HPBW of the two modes are both simulated with 32° and the peak gain of the main beam is 15.4 dBi. For the measurement, the HPBW of the Mode 2 and Mode 3 achieves 36° and 34° , respectively. The according steering angle is -39° and 36° . The system efficiencies of the two modes are measured with 172 % and 201 %.

C. Gain Compression

As an AiA, the proposed design performs non-linearity in three active modes, Mode 1, Mode 2, and Mode 3. As the input power increases, the total radiated power drops around the 1 dB compress point. The antenna system gain drops accordingly. To study the gain compression characteristic, the E-field in the far-field zone is calculated using the power density (only the main polarization is considered for simplification):

$$\begin{cases} E_{\text{slot1}} = \sqrt{2\eta \frac{P_{\text{slot1}} D_{\text{slot1}}(\theta, \phi)}{4\pi R^2}} e^{j\varphi_{\text{slot1}}} \\ E_{\text{slot3}} = \sqrt{2\eta \frac{P_{\text{slot3}} D_{\text{slot3}}(\theta, \phi)}{4\pi R^2}} e^{j\varphi_{\text{slot3}}} \\ E_{\text{slot5}} = \sqrt{2\eta \frac{P_{\text{slot5}} D_{\text{slot5}}(\theta, \phi)}{4\pi R^2}} e^{j\varphi_{\text{slot5}}} \end{cases} \quad (6)$$

where η is the vacuum wave impedance; P_{slotN} is the radiation power contributed by the Slot N; $D_{\text{slotN}}(\theta, \phi)$ is the radiation directivity of the Slot N at the direction of (θ, ϕ) ; R is the distance from the antenna phase center to the observation point; $e^{j\varphi_{\text{slotN}}}$ is the phase delay of the E-field of the Slot N. The total E-field can be represented by

$$E_{\text{total}} = E_{\text{slot1}} + E_{\text{slot3}} + E_{\text{slot5}} \quad (7)$$

Since the non-linearity comes from the active components, only P_{slot3} , and P_{slot5} items in (6) perform power compression. Based on the circuit schematic shown in Fig. 2, P_{slotN} can be calculated as:

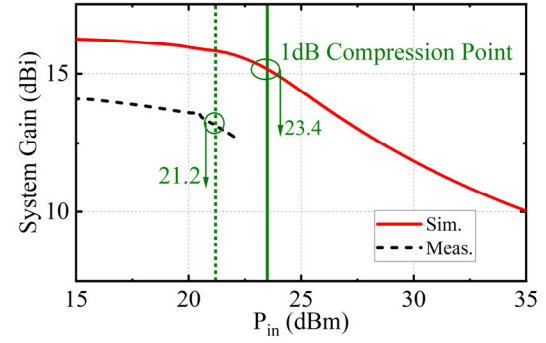


Fig. 14 Simulated and measured realized system gain of the antenna Mode 1.

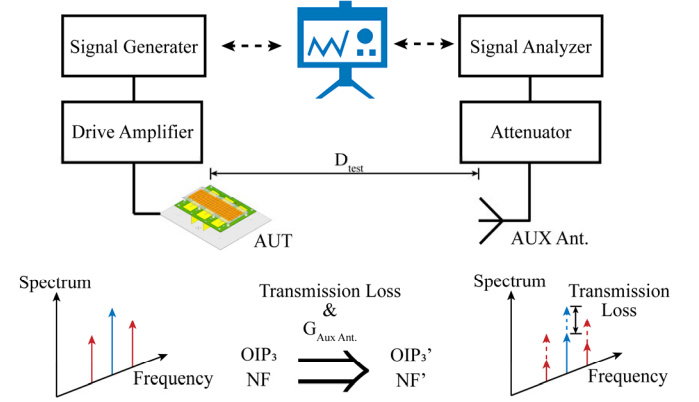


Fig. 15 Gain compression and third-order intercept point measurement setup of the reconfigurable AiA.

$$\begin{cases} P_{\text{slot1}} = e_{\text{slot1}} P_0 \\ P_{\text{slot3}} = e_{\text{slot3}} G_{\text{circuit\#1}} |S_{21}|^2 P_0 \\ P_{\text{slot5}} = e_{\text{slot5}} G_{\text{circuit\#2}} |S_{41}|^2 P_0 \end{cases} \quad (8)$$

where S_{21} and S_{41} are the coupling coefficient between the antenna port and Slot 2 or Slot 4, P_0 is the exciting power at the antenna port. Due to the symmetry of the coupling structure, $|P_{\text{slot3}}|$ is equal to $|P_{\text{slot5}}|$. The antenna system gain can be calculated and simulated based on the formula (6)-(8).

$$\begin{aligned} G_{\text{total}}(\theta, \phi) &= \frac{W_i}{W_0} = \frac{\frac{1}{2\eta} E_{\text{total}}^2}{\frac{P_0 D_0}{4\pi R^2}} \\ &= (\sqrt{e_{\text{slot1}} D_{\text{slot1}}(\theta, \phi)} e^{j\varphi_{\text{slot1}}} \\ &\quad + \sqrt{e_{\text{slot3}} G_{\text{circuit\#1}} |S_{21}|^2 D_{\text{slot3}}(\theta, \phi)} e^{j\varphi_{\text{slot3}}} \\ &\quad + \sqrt{e_{\text{slot5}} G_{\text{circuit\#2}} |S_{41}|^2 D_{\text{slot5}}(\theta, \phi)} e^{j\varphi_{\text{slot5}}})^2 \end{aligned} \quad (9)$$

Where D_0 is the directivity of the isotropic antenna. The simulated and measured realized system gain varying as the input power is given in Fig. 14. The simulated compression point referenced to the input power is 23.4 dBm. The measurement setup is depicted in Fig. 15. A high-power amplifier with a much higher saturated power is applied as the driven amplifier. The measured gain compression point is

21.2 dBm.

The total radiated power is equal to the sum of the radiated power of each slot, which omits the couple between the radiated slots. The antenna system efficiency is defined as the ratio of radiated power and the incident power:

$$e_{\text{total}} = \frac{P_{\text{radiated}}}{P_0} = e_{\text{slot1}} + e_{\text{slot3}} G_{\text{circuit\#1}} |S_{21}|^2 + e_{\text{slot5}} G_{\text{circuit\#2}} |S_{41}|^2 \quad (10)$$

Thus, the antenna system efficiency performs similar compression characteristics.

The total DC consumption of the amplifiers is measured with 1.36 W (5V, 0.272A). The DC consumption of the digital control board and the RF switches are not incorporated in the Efficiency calculation (3.3V, 30mA for control board, 3.3V 2mA for RF switches). When the antenna reaches 1 dB gain compression point, the peak power added efficiency (PAE) is 7.7 %, achieved in Mode 4. The PAE is calculated with:

$$PAE = \frac{P_{\text{active}} - P_{\text{passive}}}{P_{\text{DC}}} \quad (11)$$

where P_{active} is the radiated power of the active Mode 1, Mode 2, or Mode 3, P_{passive} is the radiated power of the Mode 0, P_{DC} is the DC power consumption. The low PAE is mainly brought by the low efficiency of the LNA in this prototype. Replacing the LNAs with the power amplifiers can obtain higher power-added efficiency.

D. Third-Order Intercept Point

Considering the symmetry of the coupling structure, the output power of Circuit#1 and Circuit#2 can be written in the form of [34]:

$$P_{\text{circuit\#1}}^{(1)} = P_{\text{circuit\#2}}^{(1)} = \frac{1}{2Z_0} a_1^2 V_{\text{in}}^2 \quad (12)$$

The according third-order intermodulation signal is [34]:

$$P_{\text{circuit\#1}}^{(3)} = P_{\text{circuit\#2}}^{(3)} = \frac{9}{32Z_0^3} a_3^2 V_{\text{in}}^6 \quad (13)$$

where $V_{\text{in}} = \sqrt{2Z_0 |S_{21}|^2 P_0} = \sqrt{2Z_0 |S_{41}|^2 P_0}$ is the incident wave voltage at the amplifier input port. $G_{\text{circuit\#1}}$ and $G_{\text{circuit\#2}}$ can be written into the product of amplifier gain G_{amp} and the loss of the circuit L_{circuit} . Thus, the total radiated signal of each slot can be rewritten as:

$$\begin{cases} P_{\text{slot1}}^{(1)} = e_{\text{slot1}} P_0 \\ P_{\text{slot3}}^{(1)} = P_{\text{slot5}}^{(1)} = e_{\text{slot3}} L_{\text{circuit\#1}} a_1^2 |S_{21}|^2 P_0 \end{cases} \quad (14)$$

The third order element is:

$$\begin{cases} P_{\text{slot1}}^{(3)} = 0 \\ P_{\text{slot3}}^{(3)} = P_{\text{slot5}}^{(3)} = e_{\text{slot3}} L_{\text{circuit\#1}} \frac{9}{4} a_3^2 (|S_{41}|^2 P_0)^3 \end{cases} \quad (15)$$

Applying formula (6) and (7), the far-field zone power density of the first-order and the third-order element derives as:

$$W_r^{(1)} = \frac{1}{2\eta} E_{\text{total}}^{(1)2} = \frac{1}{4\pi R^2} (\sqrt{e_{\text{slot1}} P_0 D_{\text{slot1}}(\theta, \phi)} e^{j\varphi_{\text{slot1}}} + \sqrt{e_{\text{slot3}} L_{\text{circuit\#1}} a_1^2 |S_{21}|^2 P_0 D_{\text{slot3}}(\theta, \phi)} e^{j\varphi_{\text{slot3}}} + \sqrt{e_{\text{slot5}} L_{\text{circuit\#2}} a_1^2 |S_{41}|^2 P_0 D_{\text{slot5}}(\theta, \phi)} e^{j\varphi_{\text{slot5}}})^2 \quad (16)$$

$$W_r^{(3)} = \frac{1}{2\eta} E_{\text{total}}^{(3)2} = \frac{e_{\text{slot3}} L_{\text{circuit\#1}} \frac{9}{4} a_3^2 (|S_{21}|^2 P_0)^3}{4\pi R^2} (\sqrt{D_{\text{slot3}}(\theta, \phi)} e^{j\varphi_{\text{slot3}}} + \sqrt{D_{\text{slot5}}(\theta, \phi)} e^{j\varphi_{\text{slot5}}})^2 \quad (17)$$

Solving $W_r^{(1)} = W_r^{(3)}$ derives the input power of the third-order intercept of the far-field zone power density. The result is simplified by the amplifier third-order intercept point $OIP_{3 \text{ AMP}}$ [34]:

$$OIP_{3 \text{ AMP}} = a_1^2 IIP_{3 \text{ AMP}} = \frac{2a_1^3}{3a_3} \quad (18)$$

So the intercept point referenced at the input port can be written as:

$$IIP_3 = \frac{OIP_3}{G_{\text{total}}} = \frac{e_{\text{slot1}} D_{\text{slot1}}(\theta, \phi) + 2a_1 |S_{21}| \sqrt{e_{\text{slot1}} D_{\text{slot1}}(\theta, \phi)} \sqrt{e_{\text{slot3}} L_{\text{circuit\#1}} D_{\text{slot3}}(\theta, \phi)} + IIP_{3 \text{ AMP}}^2}{e_{\text{slot3}} L_{\text{circuit\#1}} 9a_3^2 |S_{21}|^6 D_{\text{slot3}}(\theta, \phi)} \quad (19)$$

The IIP_3 of the active AiA is calculated based on the simulated electromagnetic field result. It can be noticed that the IIP_3 of the reconfigurable AiA achieves 34.15 dBm, which is much higher than the intercept point of the LNA (typical value is 21.4 dBm). The third-order intercept measurement setup is also shown in Fig. 15. According to the cascaded third-order intercept formula, the measured intercept point is 30.25 dBm, which can be calculated using the following formula [34]:

$$IIP_3 = IP_{3 \text{ meas}} + \text{Transmission Loss} + G_{\text{Aux Ant}} + G_{\text{AUT}}(\theta, \phi) \quad (20)$$

where $IP_{3 \text{ meas}}$ is the IP_3 directly read from the signal analyzer, Transmission loss and $G_{\text{Aux Ant}}$ are measured by a referenced antenna, $G_{\text{AUT}}(\theta, \phi)$ is the antenna gain in the observation direction.

E. Delay Spread

Since the antenna applies space power synthesis to improve the total radiated power (TRP), the different length of the each radiated path results in delay spread characteristic. The spread characteristic is similar to the multipath propagation, which leads to intersymbol interference and communication bandwidth limitation. The available bandwidth that is limited by the spread is defined as coherent bandwidth [35]:

$$B_c = \frac{1}{\sigma_t} \quad (21)$$

where σ_t is the delay spread. When the working bandwidth is narrower than the coherent bandwidth, the spread can be neglected. In the proposed design, the maximum time delay brought by the radiation path is about 1 ns. It means B_c is around 1 GHz and much larger than the impedance bandwidth and the gain bandwidth. Thus, the intersymbol interference can be ignored inside the antenna working band.

TABLE IV COMPARISON WITH THE PREVIOUS WORKS

Ref.	Function	Center Frequency (GHz)	Amplifier & Switch Type	3 dB Beamwidth (deg)	Beam Steering (deg)	System Efficiency (%)	PAE (%)	$ S_{11} $ BW (%)	Max System Gain (dBi)	Output P1dB (dBm)	Size
[11]	Tx AiA	5	HJ-FET	90	30	N.A.	46.98	2.5	11.5	-1.5	$0.83 \lambda_0 \times 0.66 \lambda_0$
[23]	Tx AiA	3.5	GaN-HEMT	N.A.	0	N.A.	65.9	5.7	15.9	38.1	$0.88 \lambda_0 \times 0.46 \lambda_0$
[36]	Tx AiA	5.8	GaN-HEMT	N.A.	0	1089	62.94	3.4	23.99	37.95	N.A.
[37]	Tx AiA	5	FET	20	0	N.A.	N.A.	>8	21.1	N.A.	$0.83 \lambda_0 \times 2.83 \lambda_0$
[1]	Beamwidth / Beam steering reconfigurable	5	PIN	40/100	± 40	81	N.A.	4	8	N.A.	$1.00 \lambda_0 \times 1.12 \lambda_0$
[6]	Beam steering reconfigurable	3.5	PIN	100/105	-11~+14	85	N.A.	5.6	4.7-6.3	N.A.	$1.17 \lambda_0 \times 1.17 \lambda_0$
[14]	Beamwidth reconfigurable	1.9	Resistor	37~136	0	N.A.	N.A.	15	5.5-9.8	N.A.	$1.00 \lambda_0 \times 1.12 \lambda_0$
[15]	Beamwidth / Beam steering reconfigurable	2	PIN	18.7/22.4	$\pm 15, -20$	N.A.	N.A.	3	14.7	N.A.	$2.30 \lambda_0 \times 2.30 \lambda_0$
[38]	Beamwidth / Beam steering reconfigurable	3.25	PIN	84~159	-20~+21	85	N.A.	10.8	7	N.A.	$0.47 \lambda_0 \times 0.47 \lambda_0$
Prop.	Quasi-duplex Reconfigurable AiA	2.45	E-pHEMT for beamwidth / CMOS for beamsteering	111	0	80.8 (Passive)	N.A.	>20	6.65	N.A.	$1.44 \lambda_0 \times 1.12 \lambda_0$
				32~36	-39, 0, 36	201 (Active)	7.7	>20	14.5	21.2	

Note: λ_0 is the free-space wavelength at the center frequency of the antenna.

N.A.: Not available

IV. EVALUATION OF SYSTEM-LEVEL PERFORMANCE

The working and application scenario of the proposed AiA is illustrated in Fig. 16. The broad beamwidth mode provides a wide coverage angle with a lower antenna gain, while the active modes are able to increase the communication distance. Thus, the combination of the four modes increases the coverage angle and distance, which guarantees good connection quality in an actual wireless communication system. A more important characteristic is that switching modes can also dynamically change the power consumption of the AiA. For short communication distances, the passive mode allows the system to work with lower power, while higher power is applied in long-distance communication. It means the base station can use the dynamic power consumption property of the antenna to build an adaptive system. In summary, the proposed work suits the IoT application that anticipates the dynamic power function to maintain low power consumption.

To better examine the coverage improvement of the AiA, the transmitting communication distance is calculated with the Friis formula. The simulation result is normalized to the communication distance of the passive Mode 0, which is shown in Fig. 17. It can be seen that the three active modes are capable to double the connection distance in the low signal-to-noise ratio environment. Besides, due to the quasi-duplexing capability of the proposed AiA, the coverage distance of Mode 0 also illustrates the receiving distance for both the passive and active modes.

V. COMPARISON WITH PREVIOUS WORKS

In this section, a brief comparison between the proposed work and the previous works is given. The AiA given in [23] is a

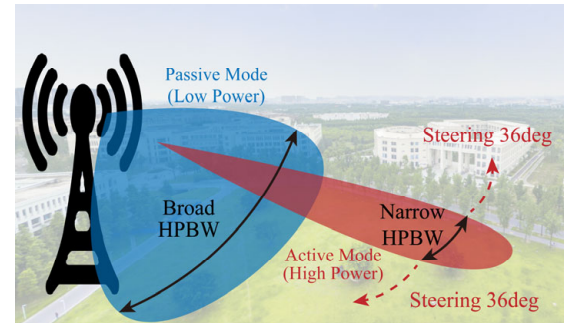


Fig. 16 Working scenario of the proposed reconfigurable AiA, both the beam width and radiation angle for the high gain case could be adjusted, which achieves real-time beam forming. Less base stations are required for the wide beamwidth case for the same coverage with less end users.

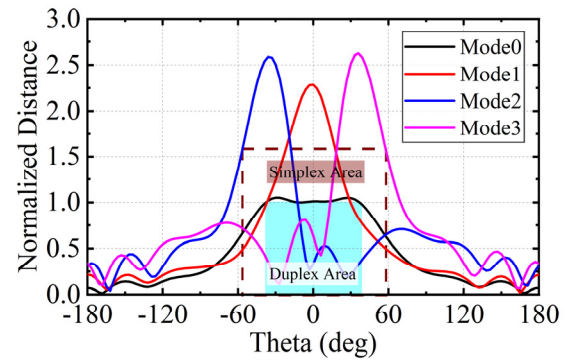


Fig. 17 Simulated communication distant comparing each mode. The result is normalized to the maximum distance of the passive mode.

conventional design that cascades an antenna and a power amplifier. It realizes high power-added efficiency but the function is very simple. The AiA proposed in [21] combines the passive antenna and the active antenna to form an array. The work mainly discusses the active component matching technique so no additional matching lump components are required. In contrast to the active antenna raised in [21], [23],

[36], [37], the proposed reconfigurable AiA novelly provides an insight that using the amplifier to realize reconfigurable AiA. Wide impedance bandwidth, HPBW reconfigurability, and quasi-duplexing characteristic prove the novelty of the work. Even though the power added efficiency shows not much advantage, which is not discussed in other references, this issue can be solved by using high-efficiency amplifiers.

In comparison to the beamwidth reconfigurable antenna, this work achieves HPBW reconfigurable range similar to [14], which is significantly higher than [1], [6], [14], [15], [38]. However, [14] failed to realize beam steering reconfigurability. The PRS antenna realizes both beam steering and HPBW reconfigurability but the tuning range is relatively narrow [15]. The work also realizes a higher antenna gain with the active integrated technique, rather than increasing the antenna size. In brief, the work paves a new access to beamwidth reconfigurability realization.

VI. CONCLUSION

This paper proposes and verifies a design of reconfigurable AiA with quasi-duplexing characteristics. The amplifiers can act as high-performance switching components and robustly control the HPBW. A discussion of using amplifiers as switches is given. The HPBW of the AiA can be configured from 32° to 111° and shows evidential advantages among other works. Two phase switching circuits provide the beam steering function, which improves the system coverage range. The switching between active and passive mode allows the system to adaptively alter power consumption while maintaining good connection quality. This ability is greatly anticipated for power-sensitive IoT devices. The simulation is based on the electromagnetic field and circuit co-simulation for high precision. The antenna prototype is fabricated and measured. The antenna exhibits good linear polarized radiation. Good agreement between the simulation and the measurement is obtained. The nonlinearity parameters, including gain compression and intermodulation, are analyzed for system design. The paper verifies that the reconfigurable AiA is a vigorous candidate for the dynamic power-control base station application demanding beam forming.

ACKNOWLEDGMENT

The authors would like to express their gratitude to professor Fei You, graduate student Jiayan Wu, Cheng Zhong, and Ce Shen for their support in active parameter measurements and discussions.

REFERENCES

- [1] Md. A. Towfiq, I. Bahceci, S. Blanch, J. Romeu, L. Jofre, and B. A. Cetiner, "A reconfigurable antenna with beam steering and beamwidth variability for wireless communications," *IEEE Trans. Antennas Propag.*, vol. 66, no. 10, pp. 5052–5063, Oct. 2018, doi: 10.1109/TAP.2018.2855668.
- [2] 5G Americas Advanced Antenna Systems for 5G White Paper. 5G Americas. Accessed: May 31, 2021. [Online]. Available: https://www.5gamericas.org/wp-content/uploads/2019/08/5G-Americas_Advanced-Antenna-Systems-for-5G-White-Paper.pdf
- [3] M. Wang *et al.*, "Miniaturization of frequency-reconfigurable antenna using periodic slow-wave structure," *IEEE Trans. Antennas Propag.*, vol. 69, no. 11, pp. 7889–7894, Nov. 2021, doi: 10.1109/TAP.2021.3076570.
- [4] Q. H. Dang, S. J. Chen, D. C. Ranasinghe, and C. Fumeaux, "A frequency-reconfigurable wearable textile antenna with one-octave tuning range," *IEEE Trans. Antennas Propag.*, vol. 69, no. 12, pp. 8080–8089, Dec. 2021, doi: 10.1109/TAP.2021.3083826.
- [5] S.-C. Tang, X.-Y. Wang, and J.-X. Chen, "Low-profile frequency-reconfigurable dielectric patch antenna and array based on new varactor-loading scheme," *IEEE Trans. Antennas Propag.*, vol. 69, no. 9, pp. 5469–5478, Sep. 2021, doi: 10.1109/TAP.2021.3060053.
- [6] W. Deng, X. Yang, C. Shen, J. Zhao, and B. Wang, "A dual-polarized pattern reconfigurable Yagi patch antenna for microbase stations," *IEEE Trans. Antennas Propag.*, vol. 65, no. 10, pp. 5095–5102, Oct. 2017, doi: 10.1109/TAP.2017.2741022.
- [7] L. Ge and K. M. Luk, "Beamwidth reconfigurable magneto-electric dipole antenna based on tunable strip grating reflector," *IEEE Access*, vol. 4, pp. 7039–7045, 2016, doi: 10.1109/ACCESS.2016.2615947.
- [8] L. Ge and K.-M. Luk, "Linearly polarized and dual-polarized magneto-electric dipole antennas with reconfigurable beamwidth in the H-plane," *IEEE Trans. Antennas Propag.*, vol. 64, no. 2, pp. 423–431, Feb. 2016, doi: 10.1109/TAP.2015.2505000.
- [9] Y. You, K. L. Ford, J. M. Rigelsford, and T. O'Farrell, "Systems analysis of a pattern reconfigurable antenna for capacity improvement of cell edge users in cellular networks," *IEEE Trans. Veh. Technol.*, vol. 67, no. 12, pp. 11848–11857, Dec. 2018, doi: 10.1109/TVT.2018.2875780.
- [10] Y. Shi, Y. Cai, J. Yang, and L. Li, "A magnetoelectric dipole antenna with beamwidth reconfiguration," *IEEE Antennas Wirel. Propag. Lett.*, vol. 18, no. 4, pp. 621–625, Apr. 2019, doi: 10.1109/LAWP.2019.2898911.
- [11] A. Khidre, F. Yang, and A. Z. Elsherbeni, "Reconfigurable microstrip antenna with tunable radiation beamwidth," in *2013 IEEE Antennas and Propagation Society Inter. Symp. (APSURSI)*, Jul. 2013, pp. 1444–1445, doi: 10.1109/APS.2013.6711381.
- [12] B. Feng, Y. Tu, K. L. Chung, and Q. Zeng, "A beamwidth reconfigurable antenna array with triple dual-polarized magneto-electric dipole elements," *IEEE Access*, vol. 6, pp. 36083–36091, 2018, doi: 10.1109/ACCESS.2018.2851992.
- [13] Y. Ji, L. Ge, J. Wang, Q. Chen, and W. Wu, "Differentially-fed aperture-coupled magneto-electric dipole antenna with continuously variable beamwidth," *IEEE Open J. Antennas Propag.*, vol. 1, pp. 165–174, 2020, doi: 10.1109/OJAP.2020.2987929.
- [14] L. Ge and K. M. Luk, "A three-element linear magneto-electric dipole array with beamwidth reconfiguration," *IEEE Antennas Wirel. Propag. Lett.*, vol. 14, pp. 28–31, 2015, doi: 10.1109/LAWP.2014.2354692.
- [15] T. Debogović and J. Perruisseau-Carrier, "Array-fed partially reflective surface antenna with independent scanning and beamwidth dynamic control," *IEEE Trans. Antennas Propag.*, vol. 62, no. 1, pp. 446–449, Jan. 2014, doi: 10.1109/TAP.2013.2287018.
- [16] C.-H. Wu and T.-G. Ma, "Pattern-reconfigurable self-oscillating active integrated antenna with frequency agility," *IEEE Trans. Antennas Propag.*, vol. 62, no. 12, pp. 5992–5999, Dec. 2014, doi: 10.1109/TAP.2014.2361897.
- [17] C.-H. Wu and T.-G. Ma, "Miniaturized self-oscillating active integrated antenna with quasi-isotropic radiation," *IEEE Trans. Antennas Propag.*, vol. 62, no. 2, pp. 933–936, Feb. 2014, doi: 10.1109/TAP.2013.2289942.
- [18] K. Wang, A. Ghiotto, L. Guo, F. Zhu, and K. Wu, "A low pulling effect self-isolated harmonic active radiator for millimeter-wave internet-of-things applications," *IEEE Trans. Antennas Propag.*, vol. 68, no. 1, pp. 171–182, Jan. 2020, doi: 10.1109/TAP.2019.2938709.
- [19] S. N. Nallandhigal, Y. Lu, and K. Wu, "Unified integration space of multi-fet active frequency multiplier and multiport antenna," *IEEE Microw. Wirel. Compon. Lett.*, vol. 30, no. 4, pp. 429–432, Apr. 2020, doi: 10.1109/LMWC.2020.2976497.
- [20] Cabria, Garcia, Malaver, and Tazon, "A PHEMT frequency doubling active antenna with BPSK modulation capability," *IEEE Antennas Wirel. Propag. Lett.*, vol. 3, pp. 310–313, 2004.
- [21] S. N. Nallandhigal and K. Wu, "Unified and integrated circuit antenna in front end—a proof of concept," *IEEE Trans. Microw. Theory Tech.*, vol. 67, no. 1, pp. 347–364, Jan. 2019.
- [22] S. N. Nallandhigal, P. Burasa, and K. Wu, "Deep integration and topological cohabitation of active circuits and antennas for power amplification and radiation in standard CMOS," *IEEE Trans. Microw. Theory Tech.*, vol. 68, no. 10, pp. 4405–4423, Oct. 2020.
- [23] Y. Lu *et al.*, "Seamless integration of active antenna with improved power efficiency," *IEEE Access*, vol. 8, pp. 48399–48407, 2020, doi: 10.1109/ACCESS.2020.2978906.
- [24] W.-C. Liao, R. Maaskant, T. Emanuelsson, V. Vassilev, O. Iupikov, and M. Ivashina, "A directly matched PA-integrated K-band antenna for

- efficient mm-wave high-power generation,” *IEEE Antennas Wirel. Propag. Lett.*, vol. 18, no. 11, pp. 2389–2393, Nov. 2019.
- [25] M. S. Sharawi, S. K. Dhar, O. Hammi, and F. M. Ghannouchi, “Miniaturised active integrated antennas: a co-design approach,” *IET Microw. Antennas Propag.*, vol. 10, no. 8, pp. 871–879, Jun. 2016.
- [26] Y. A. Atesal, B. Cetinoneri, M. Chang, R. Alhalabi, and G. M. Rebeiz, “Millimeter-wave wafer-scale silicon BiCMOS power amplifiers using free-space power combining,” *IEEE Trans. Microw. Theory Tech.*, vol. 59, no. 4, pp. 954–965, Apr. 2011.
- [27] L. Belostotski, B. Veidt, K. F. Warnick, and A. Madanayake, “Low-noise amplifier design considerations for use in antenna arrays,” *IEEE Trans. Antennas Propag.*, vol. 63, no. 6, pp. 2508–2520, Jun. 2015.
- [28] D. Segovia-Vargas, D. Castro-Galan, L. E. Garcia-Munoz, and V. Gonzalez-Posadas, “Broadband active receiving patch with resistive equalization,” *IEEE Trans. Microw. Theory Tech.*, vol. 56, no. 1, pp. 56–64, Jan. 2008.
- [29] K. F. Warnick and M. A. Jensen, “Optimal noise matching for mutually coupled arrays,” *IEEE Trans. Antennas Propag.*, vol. 55, no. 6, pp. 1726–1731, Jun. 2007.
- [30] Marianna. V. Ivashina, “Joint design and co-integration of antenna-IC systems,” in *2019 13th European Conference on Antennas and Propagation (EuCAP)*, Mar. 2019, pp. 1–7.
- [31] Qorvo, “TQP3M9035 datasheet,” Nov. 2020. <https://www.qorvo.com/products/p/TQP3M9035> (accessed May 07, 2021).
- [32] P. D. Grant, M. W. Denhoff, and R. R. Mansour, “A comparison between RF MEMS switches and semiconductor switches,” in *2004 International Conference on MEMS, NANO and Smart Systems (ICMENS’04)*, Aug. 2004, pp. 515–521.
- [33] Z. Wang, T. Liang and Y. Dong, “Composite right-/left-handed-based, compact, low-profile, and multifunctional antennas for 5G applications,” *IEEE Trans. Antennas Propag.*, vol. 69, no. 10, pp. 6302–6311, Oct. 2021, doi: 10.1109/TAP.2021.3076215.
- [34] David M. Pozar, *Microwave engineering* (fourth edition), New York, Addison-Wesley, 2011.
- [35] A. Grami, “Wireless communications,” in *Introduction to Digital Communications*, Elsevier, 2016, pp. 493–527. doi: 10.1016/B978-0-12-407682-2.00012-0.
- [36] N. Hasegawa and N. Shinohara, “C-band active-antenna design for effective integration with a GaN amplifier,” *IEEE Trans. Microw. Theory Tech.*, vol. 65, no. 12, pp. 4976–4983, Dec. 2017.
- [37] S. N. Nallandhigal and K. Wu, “Analysis and impact of port impedances on two-port networks and its application in active array antenna developments,” *IEEE Trans. Microw. Theory Tech.*, vol. 69, no. 4, pp. 2357–2370, Apr. 2021.
- [38] G.-W. Yang, J. Li, B. Cao, D. Wei, S.-G. Zhou, and J. Deng, “A compact reconfigurable microstrip antenna with multidirectional beam and multipolarization,” *IEEE Trans. Antennas Propag.*, vol. 67, no. 2, pp. 1358–1363, Feb. 2019, doi: 10.1109/TAP.2018.2883663.

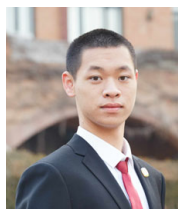
antennas. He has published more than 30 papers and 5 patents, including 17 papers on IEEE Transaction on Antennas and Propagation. He has also received multiple awards including multiple National Scholarship, and the gold medal in the 7th “Internet Plus” Innovation and Entrepreneurship worldwide Competition. He is serving as a reviewer for IEEE Transaction on Antennas and Propagation.



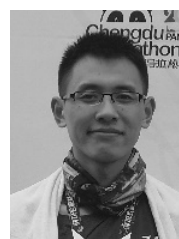
Yuandan Dong (Senior Member, IEEE) received the B.S. and M.S. degrees from the Department of Radio Engineering, Southeast University, Nanjing, China, in 2006 and 2008, respectively, and the Ph.D. degree from the Department of Electrical Engineering, University of California at Los Angeles (UCLA), Los Angeles, CA, USA, in 2012.

From September 2008 to June 2012, he was a Graduate Student Researcher with the Microwave Electronics Laboratory, UCLA. From September 2012 to February 2016, he was working as a Senior Engineer with the Research and Development Hardware Department, Qualcomm, San Diego, CA, USA. From February 2016 to December 2017, he was working as a Staff Engineer with Universal Electronics Inc., Santa Ana, CA, USA. Since December 2017, he has been a Full Professor with the University of Electronic Science and Technology of China (UESTC), Chengdu, China. He has authored or coauthored more than 200 journal articles and conference papers, which receive more than 4500 citations. He holds more than 70 patents including six international patents. He and his team have developed multiple RF products including acoustic wave filters, antenna tuners, and antennas, which are very widely shipped and applied in mobile devices. His research interests include the characterization and development of RF and microwave components, RF modules, circuits, antennas, acoustic-wave filters, and metamaterials.

Dr. Dong was a recipient of the Best Student Paper Award from 2010 IEEE Asia Pacific Microwave Conference (APMC) held in Yokohama, Japan, the Best Paper Award in 2021 IEEE International Wireless Symposium (IWS), the Distinguished Expert Presented by Sichuan Province and by China Government, respectively, and the High Level Innovative and Entrepreneurial Talent presented by Jiangsu Province. He has been a TPC member for several international conferences. He is serving as an Associate Editor for the IEEE TRANSACTIONS ON ANTENNAS AND PROPAGATION and the IEEE OPEN JOURNAL OF ANTENNAS AND PROPAGATION. He is serving as a Reviewer for multiple IEEE and IET journals including the IEEE TRANSACTIONS ON MICROWAVE THEORY AND TECHNIQUES and the IEEE TRANSACTIONS ON ANTENNAS AND PROPAGATION.



Tian Liang (Student Member) received B.S. degree in 2021 from electronic engineering from the University of Electric Science and Technology of China (UESTC), Chengdu, China. He is currently working toward Ph.D. degree at the Department of Electrical and Computer Engineering, University of California San Diego (UCSD), La Jolla, CA, USA. His research interests include reconfigurable antenna and RF circuits.



Zhan Wang (Student Member) received the B.S. degree in electrical & information engineering (high-speed rail control) from the South West Jiao Tong University (SWJTU), Chengdu, China, in 2018, and he is currently working toward the Ph.D. degree in the University of Electric Science and Technology of China (UESTC), Chengdu, China. His research interests include miniaturized antennas and microwave devices, especially, metamaterial-based antennas and reconfigurable